Nuclear imaging of the fuel assembly in ignition experiments

G. Grim, N. Guler, F. Merrill, G. Morgan, C. Danly, P. Volegov, C. Wilde, D. Wilson, D. Clark, O. Jones, K. Raman, N. Izumi, D. Fittinghoff, O. Drury, E. T. Alger, P. A. Arnold, R. C. Ashabranner, L. J. Atherton, M. A. Barrios, S. Batha, P. M. Bell, R. Benedetti, L. A. Bernstein, L. Berzins, R. Betti, S. D. Bhandarkar, R. M. Bionta, D. L. Blueuel, T. R. Boehly, E. J. Bond, M. W. Bowers, D. K. Bradley, S. G. Brass, G. K. Brunton, R. A. Buckles, S. C. Burkhart, R. F. Burr, J. A. Caggiano, D. A. Callahan, D. T. Casey, C. Castro, P, M, Celliers, C. J. Cerjan, G. A. Chandler, C. Choate, D. S. Clark, S. J. Cohen, G. W. Collins, G. W. Cooper, J. Craddick, P. S. Datte, E. L. Dewald, P. Di Nicola, J. M. Di Nicola, L. Divol, S. N. Dixit, R. Dylla-Spears, J. M. Dzenitis, E. G. Dzenitis, et al.

Disclaimer

Nuclear imaging of the fuel assembly in ignition experiments

G. Grim,[1, a)] N. Guler,[1] F. Merrill,[1] G. Morgan,[1] C. Danly,[1] P. Volegov,[1] C. Wilde,[1] D. Wilson,[1] D. Clark,[2] O. Jones,[2] K. Raman,[2] N. Izumi,[2] D. Fittinghoff,[2] O. Drury,[2] E. T. Alger,[2] P. A. Arnold,[2] R. C. Ashabranner,[2] L. J. Atherton,[2] M. A. Barrios,[2] S. Batha,[1] P. M. Bell,[2] R. Benedetti,[2] R. L. Berger,[2] L. A. Bernstein,[2] L. Berzins,[2] R. Betti,[3] S. D. Bhandarkar,[2] R. M. Bionta,[2] D. L. Blueuel,[2] T. R. Boehly,[3] E. J. Bond,[2] M. W. Bowers,[2] D. K. Bradley,[2] S. G. Brass,[2] G. K. Brunton,[2] R. A. Buckles,[4] S. C. Burkhart,[2] R. F. Burr,[2] J. A. Caggiano,[2] D. A. Callahan,[2] D. T. Casey,[2] C. Castro,[2] P. M. Celliers,[2] C. J. Cerjan,[2] G. A. Chandler,[5] C. Choate,[2] D. S. Clark,[2] S. J. Cohen,[2] G. W. Collins,[2] G. W. Cooper,[6] J. R. Cox,[2] J. Craddick,[4] P. S. Datte,[2] E. L. Dewald,[2] P. Di Nicola,[2] J. M. Di Nicola,[2] L. Divol,[2] S. N. Dixit,[2] R. Dylla-Spears,[2] J. M. Dzenitis,[2] E. G. Dzenitis,[2] M. J. Eckart,[2] D. C. Eder,[2] D. H. Edgell,[3] M. J. Edwards,[2] J. H. Eggert,[2] R. B. Ehrlich,[2] G. V. Erbert,[2] J. Fair,[2] D. R. Farley,[2] B. Felker,[2] R. J. Fortner,[2] J. A. Frenje,[7] G. Frieders,[2] S. Friedrich,[2] M. Gatu Johnson,[7] C. Gibson,[2] E. Giraldez,[8] V. Y. Glebov,[1] S. M. Glenn,[2] S. H. Glenzer,[2] G. Gururangan,[2] S. W. Haan,[2] K. D. Hahn,[5] B. A. Hammel,[2] A. V. Hamza,[2] E. P. Hartouni,[2] R. Hatarik,[2] S. P. Hatchett,[2] C. Haynam,[2] G. Heestand,[2] M. R. Hermann,[2] H. W. Herrmann,[1] D. G. Hicks,[2] D. E. Hinkel,[2] J. P. Holder,[2] J. B. Horner,[2] W. W. Hsing,[2] H. Huang,[2] M. C. Jackson,[2] K. S. Jancaitis,[2] M. G. Johnson,[7] D. H. Kalantar,[2] R. L. Kauffman,[2] M. Kauffman,[9] J. D. Kilkenny,[8] J. R. Kimbrough,[2] R. Kirkwood,[2] J. L. Kline,[1] J. J. Klingman,[2] J. P. Knauer,[3] K. M. Knittel,[2] J. A. Koch,[2] T. R. Kohut,[2] B. J. Kozioziemski,[2] K. Krauter,[2] G. W. Krauter,[2] A. L. Kritcher,[2] J. Kroll,[2] G. A. Kyrala,[1] K. N. La Fortune,[2] G. LaCaille,[2] L. J. Lagin,[2] T. A. Land,[2] O. L. Landen,[2] D. W. Larson,[2] D. A. Latray,[2] R. J. Leeper,[5] S. LePape,[2] J. D. Lindl,[2] R. R. Lowe-Webb,[2] T. Ma,[2] B. J. MacGowan,[2] A. J. MacKinnon,[2] A. G. MacPhee,[2] R. A. Malone,[9] T. N. Malsbury,[2] E. Mapoles,[2] C. D. Marshall,[2] D. G. Mathisen,[2] G. N. McHalle,[2] P. McKenty,[3] J. McNaney,[2] N. B. Meezan,[2] P. Michel,[2] J. L. Milovich,[2] J. D. Moody,[2] A. S. Moore,[10] M. J. Moran,[2] K. Moreno,[8] E. I. Moses,[2] D. H. Munro,[2] B. R. Nathan,[2] A. G. Nelson,[6] A. Nikroo,[8] R. E. Olson,[5] C. Orth,[2] A. E. Pak,[2] E. S. Palma,[2] N. E. Palmer,[2] T. G. Parham,[2] P. K. Patel,[2] R. W. Patterson,[2] R. D. Petrasso,[7] R. Prasad,[2] J. E. Ralph,[2] S. P. Regan,[3] M. J. Richardson,[2] H. Rinderknecht,[7] H. F. Robey,[2] G. F. Ross,[2] C. L. Ruiz,[5] F. H. Séguin,[7] J. D. Salmonsen,[2] T. C. Sangster,[3] J. D. Sater,[2] R. L. Saunders,[2] M. B. Schneider,[2] D. H. Schneider,[2] M. J. Shaw,[2] N.

Simanovskaia,[2] B. K. Spears,[2] P. T. Springer,[2] C. Stoeckl,[3] W. Stoeffl,[2] L. J. Suter,[2] C. A. Thomas,[2] R. Tommasini,[2] R. P. Town,[2] A Traille,[4] B. Van Wonterghem,[2] R. J. Wallace,[2] S. Weaver,[2] S. V. Weber,[2] P. J. Wegner,[2] P. K. Whitman,[2] K. Widmann,[2] C. C. Widmayer,[2] R. D. Wood,[2] B. K. Young,[2] R. A. Zacharias,[2] and A. Zylstra[7]

[1] *Los Alamos National Laboratory, Los Alamos, New Mexico 87545, USA*

[2] *Lawrence Livermore National Laboratory, Livermore, California 94551, USA*

[3] *Laboratory for Laser Energetics, Univ. of Rochester, Rochester, New York 14623, USA*

[4] *National Securities Technologies, LO, Livermore, California 94550, USA*

[5] *Sandia National Laboratory, Albuquerque, New Mexico 87123, USA*

[6] *Chemical and Nuclear Engineering Department, University of New Mexico, Albuquerque, New Mexico 87131, USA*

[7] *Plasma Science and Fusion Center, Massachusetts Institute of Technology, Cambridge, Massachusetts 2139, USA*

[8] *General Atomics, San Diego, California 92186, USA*

[9] *National Securities Technologies, LAO, Los Alamos, New Mexico 87544, USA*

[10] *AWE, Aldermaston, Reading, Berkshire, RG7 4PR, United Kingdom*

(Dated: 11 December 2012)

Nuclear imaging data collected during the National Ignition Campaign (NIC) at the National Ignition Facility (NIF) from Dec. 2011 through Aug 2012 are reported. The data include the size and shape of the hot-spot and cold-fuel using images of neutrons in the windows 13-17 MeV and 6-12 MeV respectively. The fuel configuration is defined by Legendre polynomial fits of the contours at 17% of peak intensity. Volumes are defined by the surface of revolution about the hohlruam axis using the fit contours. The average fuel assembly near stagnation is characterized by a central hot oblate spheroid of mean radius $P_0^{hs} = 27.4\mu$m, ($\sigma_{rms} = 2.4 \ \mu$m), with a mean polar deviation of -4.4 μ, or P_2^{hs}/P_0^{hs} = -0.15 (($\sigma_{rms} = 0.16$). X-ray self-emission images, as well as simulated neutron images, show good agreement with the nuclear image data with: $P_0^{X-ray} = 27.3\mu$m, ($\sigma_{rms}^{X-ray} = 2.6 \ \mu$m), P_2^{X-ray}/P_0^{X-ray} = -0.09 (($\sigma_{rms}^{X-ray} = 0.08$), and $P_0^{sim} = 26.4\mu$m, ($\sigma_{rms}^{sim} = 1.8 \ \mu$m), with P_2^{sim}/P_0^{sim} = -0.01 (($\sigma_{rms}^{sim} = 0.18$). Surrounding the hot-spot is a dense sphere of deuterium-tritium fuel with a mean radius of P_0^{cf} = 41 μm ($\sigma_{rms} = 3.9 \ \mu$m), which is smaller than 2-D post-shot simulation values of P_0^{cf} = 45 μm ($\sigma_{rms} = 2.8 \ \mu$m). The image data, combined with other nuclear data is used calculate a "geometric" down scattered neutron ratio. The geometric down scatter ratio is on average 37% larger than time-of-flight measurements. The mean post-shot simulated down scatter ratio is systematically larger 27% than data. Preliminary studies indicate the down scattered rate differences are consistent with significant deuterium-tritium mass, $\gtrsim$ 20% of initial, outside the 17% of peak density contour, due either to low mode mass asymmetry, or high mode mix at the ablator ice interface.

56

a)gpgrim@lanl.gov

I. INTRODUCTION

The goal of indirectly driven inertial confinement fusion experiments at the National Ignition Facility (NIF) is to obtain thermonuclear ignition using a small mass, ~ 170 μg, of hydrogen isotopes.[1] The process begins with the 192 beam, 351 nm, NIF laser which illuminates a high-Z cavity (hohlraum) producing a flux of soft X-rays at a temperature of $\sim$290 eV. These X-rays ablate the outer surface of a $\sim$2 mm diameter plastic shell, or ablator, containing a cryogenically formed deuterium-tritium ice shell on the inner surface, approximately 70 μm thick. As the outside of the ablator is accelerated outwards, the balance of the mass recoils inward, compressing the remnant deuterium-tritium vapor, formed at the 19.8 K triple point prior to implosion. The assembly accelerates through a peak velocity of $\sim$300 Km/s, before decelerating and stagnating, compressed by a factor of almost 30. The **pdV** work performed on the vapor raises the central temperature of the assembly to ~ 3 keV, initiating $T(d,n)\alpha$ reactions. The goal is to initiate a propagating a wave of fusion reactions in the surrounding dense deuterium-tritium shell via sustained heating through alpha-particle energy deposition. To optimize the experimental program, the National Ignition Campaign (NIC) was created with a defined set of goals, requirements, and experimental plans.[2–4] During 2011, initial results from NIC experiments with cryogenically layered targets were published.[5,6]

Additional results from ignition experiments performed between December 2011 and August 2012 are reported here. The results focus on nuclear performance with emphasis on the shape of the implosion using the neutron imaging diagnostic.[7–10] Rather than focus on detailed analysis of one or two specific shots, as reported by Cerjan[11], we report on the averages and trends of the 2012 data set. In section II we briefly describe the neutron imaging technique, including image formation, and reconstruction. In section III we describe the simple geometric model of the fuel assembly using the neutron imaging data and define the geometric down scatter ratio. In section IV we report on the fuel assembly geometry data from 2012 ignition experiments and compare these to post-shot simulations. A summary of the results and conclusions of these studies is presented in section V.

II.   NEUTRON IMAGING

A.   Overview

Detailed aspects of the development and implementation of the NIF neutron imaging diagnostic has been documented in a number publications[7–10]. Presented is a brief overview of the system.

B.   Image Formation

The primary task of the NIF neutron image diagnostic is to produce 2-D images of where neutrons are produced and scattered within the deuterium-tritium volume of layered cryogenic implosions at the the NIF. The original specifications[12] for the system require two neutron images, one of neutrons with a kinetic energies in the range 13.5 to14.5 MeV, the primary neutron image, and one with neutron energies in the range 6 to 10 MeV, the scattered neutron image. Further, images must be collected at primary yields of 1E15 neutrons with a "point resolution" no worse than 15 μm.

To achieve these goals the system was designed with a compound aperture, a "grand array[13]" of 20 pinholes combined with 3 penumbral apertures. The apertures are formed in 20 cm long gold foils, that are supported by faced tungsten plates to provide mechanical stability.[14] To address the competing requirements of manufacturability and image performance, the pinholes were made using a triangular cross section. The average diameter of the pinholes for 14 MeV neutrons is 19 μm. To accommodate a field of view that is twice the source size, the front of the aperture body is located 32.5 cm from the target. The grand array of pinholes focuses to a point 26.5 cm in front of the aperture, providing tolerance to pinhole array misalignment.

Fig 1 shows the neutron imaging system detector, housed outside the NIF building, in an "annex" constructed to support the diagnostic. Neutrons enter the annex from the upper left, through the final line-of-site collimator. The neutrons then pass through a pair of neutron time-of-flight "paddle detectors," where measurements of ion temperature, yield, and spectral, or scatter rate measurements, are made. Subsequently, the neutrons are detected in a 5 cm long by 16×16 cm^2 organic scintillator, constructed from a coherent array of 250 μm diameter scintillating fibers. Recoil lengths of elastically scattered protons
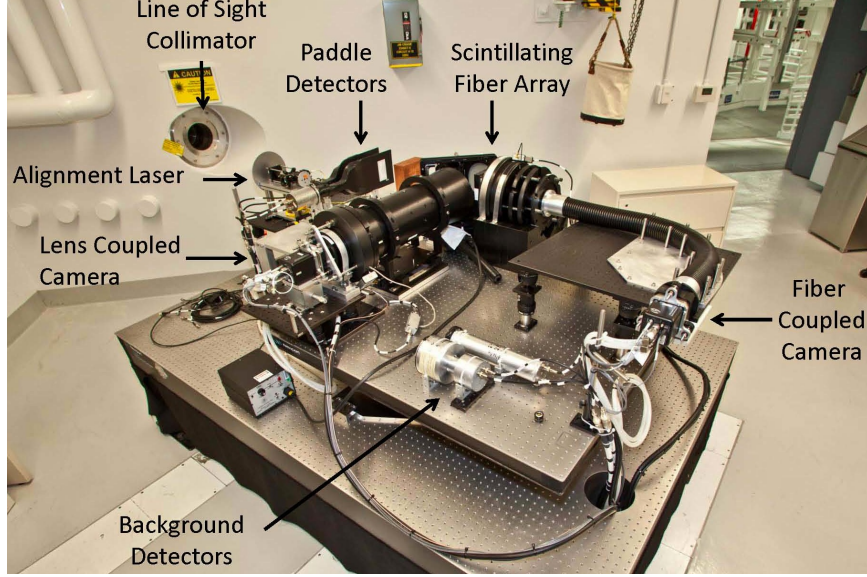
5

FIG. 1: The detector system for the NIF neutron imaging diagnostic. Neutron exit the collimated line-of-site in the upper left, pass through the time-of-flight paddles, and are imaged in the scintillating fiber array, indicated by the arrows.

can extend several millimeters in the scintillator, thus the imaging scintillator mid-plane is positioned 2802.5 cm from the target providing a system magnification of 85.2 for a pinhole images, and resulting in a recording system resolution of 14.5 μm at the target plane. To capture two images, light from each end of the fiber array is collected and optically relayed to CCD camera systems where it is digitized. Each optical relay leg includes electro-optic shuttering using micro channel plate image intensifiers (MCPII) to record images of neutrons with different kinetic energies. In the data reported below, neutrons are typically collected in energy bands from 13-17 MeV, primary neutron images, and 6-12 MeV, scattered neutron images. The energy gate change from the original system requirements do not affect the primary data interpretation goals for these two images, but allow wider gates that provide better camera system performance.

C.   Image Processing

To prepare the data for physics analysis, images must be corrected for both instrument and image formation effects. Correction for instrument effects, include electronic pedestal subtraction and star removal, as well as position dependent sensitivity corrections (flat-

6

field) and spatial dewarpring of the image field. The image data from the two cameras are absolutely registered to a precision of ± 2.5 μm at the object plane. To correct for the residual primary image still present during the scattered image gate, 1.4% of the primary image is subtracted from the scattered image. Long range blur, *i.e.* light outside the images produced by multiply scattered neutrons, is subtracted using a fit to the inter-aperture light field, assuming the blur source originates from neutrons passing through the penumbral apertures.

After instrument and image formation corrections are applied, the array of images are analyzed to determine the position of the source relative to each aperture centerline. The set of pinholes most closely pointed to the source are input to an Expectation Maximization algorithm.[15–17] The algorithm corrects for the non-stationary aperture point spread function, as well as filtering the image to reduce high frequency noise in the object field.

The NIF neutron imaging diagnostic has been under development for many years, with formal work dating to 2005.[8] During this time a wide range of experimental and computer simulation studies have been performed to define and quantify the NIF neutron imaging system resolution. In previous work[9] the system point resolution, accounting for image formation and inversion at NIF relevant signals levels was determined to be 18 μm.

III.   FUEL ASSEMBLY DESCRIPTION

As mentioned, the primary imaging task is to determine where neutrons are produced and scattered within the deuterium-tritium fuel. The goal is to create a simple model of the fuel assembly near stagnation, illustrated in Fig. 2a. By creating a 3-D model, it is possible to infer, volumes, densities, pressures, etc. and to thereby evaluate the hydrodynamic performance of the experiment, *c.f* the work of Cerjan and Springer.[11] In this model two characteristic regions are identified, the central hot ($\sim$ 2-4 keV) core where fusion reactions occur, and the surrounding cold, dense deuterium-tritium shell, the main fuel payload and scattering source within the assembly. To create this model of the fuel assembly from the 2-D images distributions, surfaces of revolution, defined by contours of constant signal intensity are constructed. The NIF neutron imaging system views the imploded capsule in the equatorial plane, orthogonal to the hohlraum axis, as illustrated in Fig. 2b, therefore this axis is the center of revolution for volume construction.

7

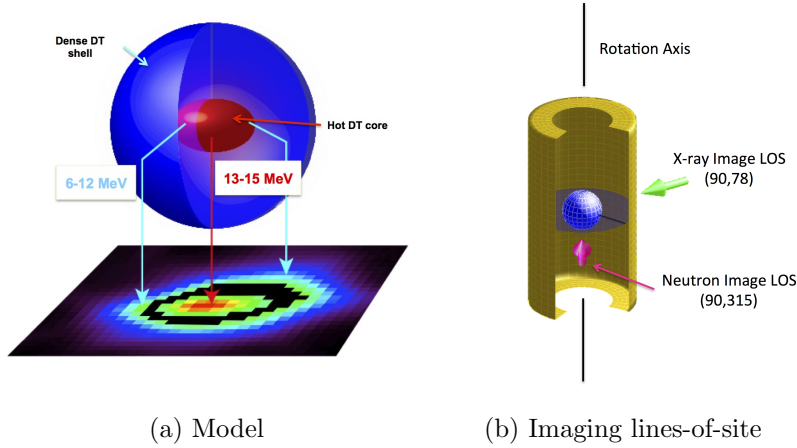(a) Model   (b) Imaging lines-of-site

FIG. 2: Fig. 2a illustrates the simple 3-D fuel model to describe the source volumes for the neutron image data. Fig. 2b illustrates the geometry of the experiment, the axis symmetry defined by the hohlraum, and the imaging lines of site for neutrons and X-rays.

A.   The 17% contour

In image analyses at the NIF, it is common practice to define the lateral extent of a volume by a contour of constant signal intensity. For historical reasons, the contour used at 17% of peak signal intensity is the primary contour used. This contour is sufficiently weak to accurately represent the lateral extent of the source, but strong enough to be distinct from random noise outside the source. This choice is further motivated by noting that for a spherical source of radius R_0 and constant emissivity, the 1-D Abel transform is given by, $2\sqrt{R_0^2 - r^2}$. The lateral extent of this function at 17% of the peak amplitude, measures 98.5% of R_0, an adequate measure of extent. For the scattered neutron image, where no simple analytic image formation expression is available, simulated images using transport Monte Carlo tools,[18–20] indicate the 17% contour also accurately represents the lateral extent of the dense shell.

1.   Legendre Polynomial Fit

To simplify the mathematical representation of the contour, a finite Legendre polynomial expansion, *c.f.* Eqn. 1, is used, where θ is the polar angle in the plane orthogonal the

8

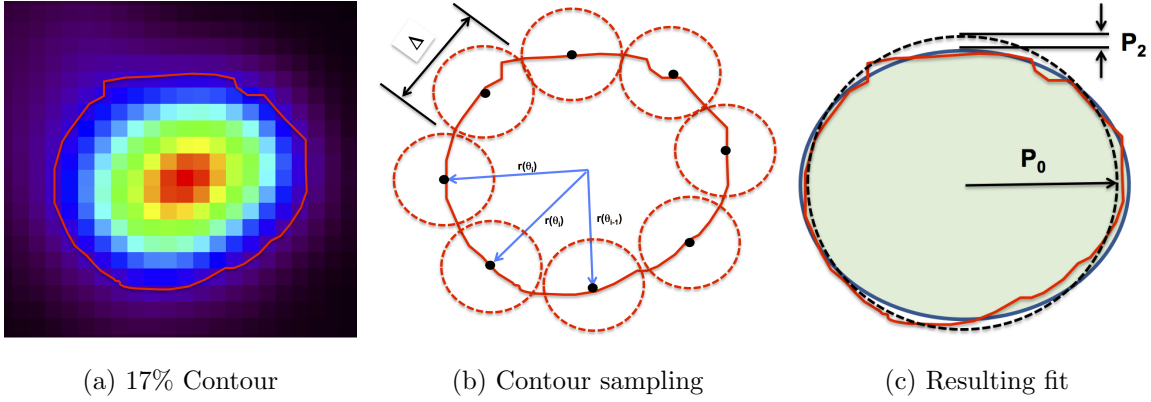(a) 17% Contour   (b) Contour sampling   (c) Resulting fit

FIG. 3: Illustration of contour fitting with finite resolution. Fig. 3a shows the 17% of peak contour, Fig. 3b, the contour is sampled with independent measures of the radial positions as a function of θ, and Fig. 3c shows the results of the fit using the first two even modes of the Legendre polynomial expansion.

174 neutron imaging line-of-site, and P_l is the lth coefficient of the Legendre polynomial L_l.

$$r_{17\%}(\theta) = \sum_{l=0}^{L} P_l \cdot L_l(\theta) \tag{1}$$

175 For the neutron imaging system the fit is performed out to mode 6, *i.e.* L = 6, with the
176 constraint that $P_1 = 0$, which determines the location of the contour center. The process of
177 the fit is illustrated in Fig. 3. Fig. 3a shows the 17% of peak contour identified on a sample
178 image. One possible set of independent samples of the contour radius as a function of θ, are
179 shown in 3b. The samples are independent if they are separated by the system resolution Δ.
180 Each sample generates a radial measurement from the position that eliminates P_1. Because
181 of the finite resolution of the system Δ, the independent samples are taken discrete angles
182 θ_i. Fig.3c shows the results of a typical fit of the Legendre polynomial expansion, with the
183 first two even modes illustrated. The parameter P_0 is the mean radius of the contour, and
184 P_2, is the deviation from this mean radius along the polar direction, or $\theta = 0$, direction. A
186 negative P_2 is smaller han the mean radius along the polar ($\theta = 0$) direction.

187   2.   *Accuracy of Legendre Coefficients*

188   This conceptual exercise allows for a simple estimate of fit parameter accuracy. To
189 estimate the P_0 accuracy, a contour is represented by the function $r(\theta) = P_0 + P_2 \cdot L_2(\theta)$, with
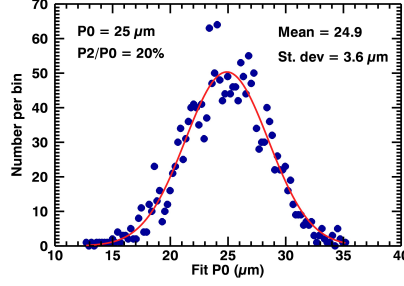
FIG. 4: Distribution of P_0 fit values from a replicate trials study.

a point resolution of Δ, the number of independent samples of this contour is approximated by the expression:

$$N_{samp} \approx \frac{2\pi\sqrt{\frac{(P_0+P_2)^2+(P_0-P_2/2)^2}{2}}}{\Delta} \qquad (2)$$

Letting Δ represent the full width at half maximum of a Gaussian distributed error on the radial measurement, then accuracy of measurement of P_0 is estimated by:

$$\delta P_0 = \frac{\Delta}{2\sqrt{2\ln 2(N_{samp}-1)}} \qquad (3)$$

For the NIF neutron imaging system, this implies that a contour with $P_0 = 30$ μm, results in 10 independent samples of the mean radius, assuming an 18 μm resolution element. The resulting accuracy of the P_0 measurement is ≈ 2.5 μm. This estimate is in good agreement with replicate trials studies, where contours of constant intensity are generated at a variety of different P_0 and P_2 values. These contours are randomly sampled with resolution size Δ and fit to the Legendre polynomial expansion using a least squares fitting algorithm. An example distribution of the resulting fits is illustrated in Fig 4. A gaussian fit to the ensemble of trials gives an estimate of δP_0 of 2.5 μm.

B.   Stagnation state variables

Using the surfaces derived from the revolved contours, volumes are calculated for the two regions. Assuming an isobaric configuration, it is possible to infer key state variables of the fuel assembly, including, density, pressure, and adiabat. Detailed modeling of the fuel assembly to infer pressure and adiabatic is described elsewhere[11]. In this work we focus on

10

208 calculating the geometry and density of the assembly, and from that the scattering rate, or
209 down scatter ratio of the assembly.

210 1. Density

211   The density of the deuterium-tritium volume producing the primary neutron yield, is
212 calculated by inverting the yield equation:

$$Y_n = n_{dt}^2 \langle \sigma \bar{v} \rangle \tau_{rh} V_{hs} \Rightarrow n_{dt} = \sqrt{\frac{Y_n}{\langle \sigma \bar{v} \rangle \tau_{rh} V_{hs}}} \tag{4}$$

213 where Y_n is the total fusion yield, n_{dt} is the number density of pairs of deuterium-tritium ions
214 (equimolar initial conditions) in units of cm^{-3}, $\langle \sigma \bar{v} \rangle$ is the velocity averaged cross section
215 in units of cm^3/s, and V_{hs} is the hot-spot volume in units of cm^3. In ignition experiments
216 at the NIF, neutron yields are often quoted as the number of neutrons in the energy range
217 from 13-15 MeV, which is lower than the fusion yield, due to scattering in the dense shell,
218 and therefore must be corrected by the measured down scatter rate.
219   The density of the deuterium-tritium shell surrounding the hot-spot, is calculated by
220 assuming the balance of the initial mass resides inside the dense shell surrounding the volume
221 producing the primary neutron, thus

$$\rho_{cf} = \frac{M_{DT}^{init} - \rho_{hs} V_{hs}}{V_{cf}}, \tag{5}$$

222 where, M_{DT}^{init} is the initial deuterium-tritium mass in the capsule, ~ 170 μg, ρ_{hs} and V_{hs} are
223 the hot-spot density and volume, respectively, and V_{cf} is the cold fuel volume.

224 2. Geometric Down Scattered Ratio

225   Assuming uniform density within each volume, the above geometry and density allow
226 calculation of the neutron scattering rate within the fuel assembly. Fig. 5 illustrates the
227 simplified fuel configuration used to calculate this rate. The assembly has been simplified to
228 two concentric spheres defined by the radii, $R_{hs} \equiv P_0^{hs}$, where fusion neutrons are born, and
229 $R_{cf} \equiv P_0^{cf}$, the dense deuterium-tritium shell where most neutrons scatter. The densities
230 of these two volumes are n_{hs}, and n_{cf} respectively. The lines shown illustrate how the how
231 the fuel volume is sampled by scattered neutrons. For a detector located at a large distance

11

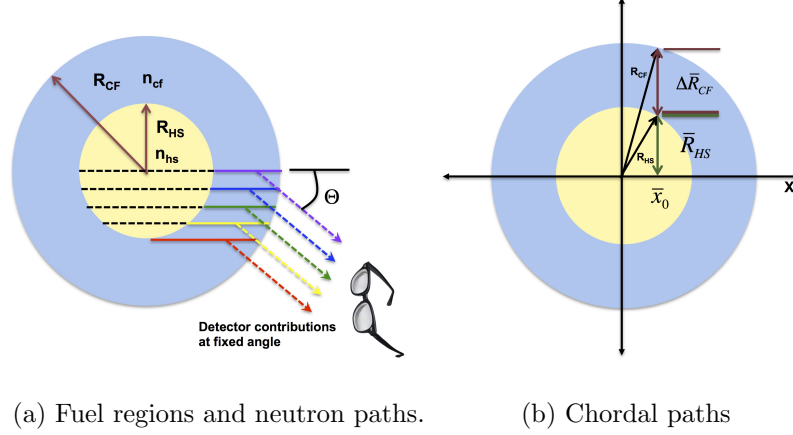(a) Fuel regions and neutron paths. (b) Chordal paths

FIG. 5: Graphical representation of how geometric down scatter ratio is calculated. See text for full description.

232 from the assembly, neutrons that scatter at a specific angle and into the detector acceptance
233 were born as neutrons traveling to the right along the dashed parallel lines through the
234 hot-spot. The neutrons may scatter at the angle θ, at any point along either the dashed line
235 through the hot-spot, or along the solid line within the cold-fuel. The energy of the scattered
236 neutron will be determined by the scattering process and the mass of the scattering center.
237 At the NIF, the down scatter ratio is calculated using the flux of neutrons between 10 to 12
238 MeV, where only elastic scattering from deuterium and tritium need be considered, and the
239 corresponding scattered neutron energy is calculated using:

$$E'_n = \frac{14.1MeV}{(A+1)^2}(\cos\theta + [A^2 - \sin^2\theta]^{1/2})^2 \tag{6}$$

240 where A is the mass of the deuterium, or tritium scattering center.

241   For a radial path through the equimolar deuterium-tritium fuel assembly, the ratio of the
242 scattered neutron flux in the 10 to 12 MeV band to the un-collided flux is given by:

$$\frac{\Phi_{coll}^{10-12}}{\Phi_{unc}} = \alpha^{10-12}\left(\exp\left\{\frac{N_A\bar{\sigma}_{dt}}{\bar{M}_{dt}}\left(\rho_{cf}\Delta R_{cf} + \rho_{hs}R_{hs}\right)\right\} - 1\right) \tag{7}$$

243 where, N_A is Avogadro's number, $\bar{M}_{dt}$ is the average molar mass of a deuterium and tritium
244 ion, $\bar{\sigma}_{dt}$ is the average elastic scattering cross section of a 14.1 MeV neutron off of deuterium
245 and tritium (= 0.77 b), ρ_{cf} and ρ_{hs} are the gram densities of the cold-fuel and hot spot
246 respectively, R_{hs} is the hot spot radius, ΔR_{cf} is the thickness of the cold fuel along the
247 radial, and finally, α^{10-12} is the fraction of scattered neutrons in the 10 to 12 MeV band,

$$\alpha^{10-12} = \frac{\int_{10}^{12} dE \frac{d\sigma}{dE}}{\int dE \frac{d\sigma}{dE}} \tag{8}$$

$$= 0.239 \tag{9}$$

249   Due to the relatively small fraction of scattered neutrons in the energy range between
250 13 to 15 MeV, the uncollided flux may be approximated by this energy band, and thus the
251 down-scattered ratio (DSR) is defined as:

$$DSR(10-12) = \frac{\Phi_{coll}^{10-12}}{\Phi^{13-15}} \approx \frac{\Phi_{coll}^{10-12}}{\Phi_{unc}}. \tag{10}$$

252   As can be seen in Fig. 5, a finite size hot-spot will generate non-radial contributions
253 to the detected flux, which isn't included in Eqn. 7 above. To address this, Eqn. 7 is
254 generalized to the mean chordal path, through the fuel assembly, $\bar{R}_{hs} + \Delta\bar{R}_{cf}$, which occurs
255 at the mean apothem x_0, in Fig. 5b. The mean apothem is the density and path length
256 weighted average of apothem across the hot-spot *i.e.*:

$$\bar{x}_0 = \frac{\int_0^{R_{hs}} dx\, x \left(n_{hs}\sqrt{R_{hs}^2 - x^2} + n_{cf}\left(\sqrt{R_{cf}^2 - x^2} - \sqrt{R_{hs}^2 - x^2}\right)\right)}{\int_0^{R_{hs}} dx \left(n_{hs}\sqrt{R_{hs}^2 - x^2} + n_{cf}\left(\sqrt{R_{cf}^2 - x^2} - \sqrt{R_{hs}^2 - x^2}\right)\right)}, \tag{11}$$

257 which reduces to:

$$\bar{x}_0 = \frac{4\left(R_{cf}^3 - \left(R_{cf}^2 - R_{hs}^2\right)^{3/2} - R_{hs}^3\left(1 - \frac{n_{hs}}{n_{cf}}\right)\right)}{6\left(R_{hs}\sqrt{R_{cf}^2 - R_{hs}^2} + R_{cf}^2\sin^{-1}\left(R_{hs}/R_{cf}\right)\right) - 3\pi R_{hs}^2\left(1 - \frac{n_{hs}}{n_{cf}}\right)}. \tag{12}$$

258 From this the mean chordal path lengths may be calculated:

$$\bar{R}_{hs} = \sqrt{R_{hs}^2 - \bar{x}_0^2}, \tag{13}$$

$$\bar{R}_{cf} = \sqrt{R_{cf}^2 - \bar{x}_0^2} - \sqrt{R_{hs}^2 - \bar{x}_0^2}. \tag{14}$$

259   Fig. 6 illustrates the accuracy of the geometric down scatter ratio formula. A series of
260 static fuel assemblies with varying radii, asymmetries, and densities, were simulated using
261 MCNP,[18] a general purpose neutron transport Monte Carlo package. The figure horizontal
262 axis is the ratio of the neutrons tallied in the 10 to 12 MeV range to the 13-15 MeV range, at
263 a position outside the fuel assembly, simulating a NIF neutron time-of-flight type of detector.
264 The vertical axis is the geometric DSR, using the fuel geometry and density configuration
265 that was simulated. The number of histories generated were large enough that the tally
266 error bars are smaller than the data marker. The red, $y = x$ line, illustrates good agreement
267 between the geometric formula and the tallied ratio over the range of down scatter values
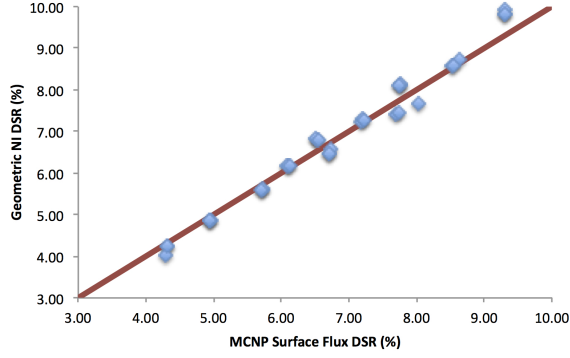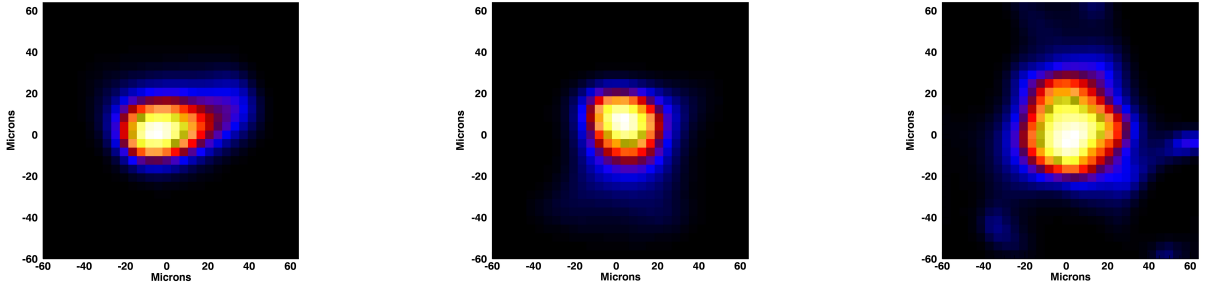268 typically observed in ignition experiments at the NIF.

FIG. 6: Comparison of the geometric down scatter ratio formula with the simulated ratio, calculated from neutron tallies using MCNP.

(a) Shot N111215: $P_0^{hs} = 28 \pm 3$ μm, (b) Shot N120321: $P_0^{hs} = 26 \pm 3$ μm, (c) Shot N120405: $P_0^{hs} = 27 \pm 3$ μm,

$P_2^{hs}/P_0^{hs} = $ -29 $\pm$ 6 % $\qquad\qquad$ $P_2^{hs}/P_0^{hs} = $ -10 $\pm$ 6 % $\qquad\qquad$ $P_2^{hs}/P_0^{hs} = $ 4 $\pm$ 6 %

FIG. 7: Gallery of primary (13-17 MeV) neutron images from layered cryogenic implosions between Dec. 2011 and Aug. 2012.

IV.   2012 IGNITION EXPERIMENT DATA

A.   The Primary Neutron Image

As described previously,[9,10] images of primary neutrons produced by deuterium-tritium fusion reactions are collected by correlating the electro-optic shutter, between the scintillator and digitizer to coincide with the arrival time of 14.1 MeV neutrons. Specifically, the primary camera collects images of neutrons between 13 and 17 MeV, a gate width of 70 ns, starting 498 ns after bang time. Fig. 7 shows a gallery of neutron images collected during the 2012 ignition campaign. The size of a pixel in these images is 4 μm. The gallery exemplifies

14

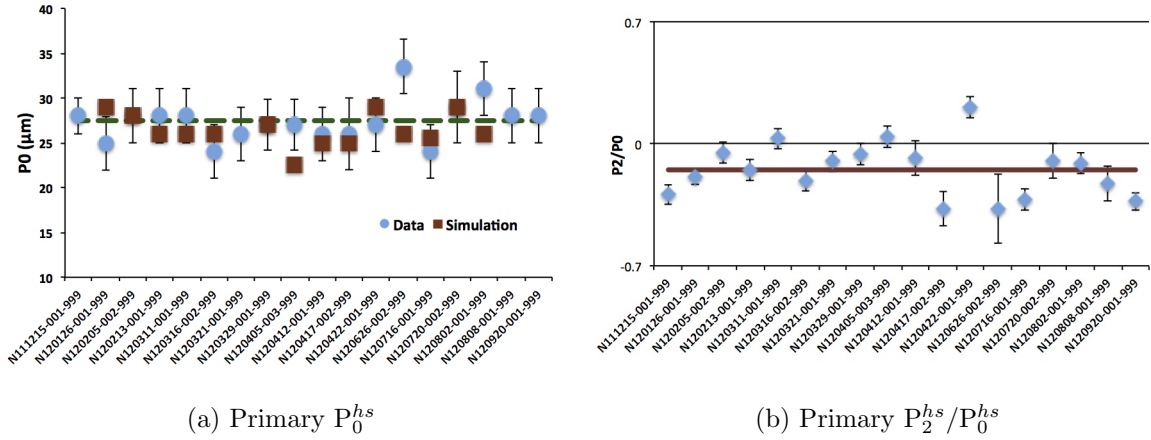(a) Primary P_0^{hs} (b) Primary P_2^{hs}/P_0^{hs}

FIG. 8: Primary neutron image data from ignition experiments between Dec. 2011 and
Aug. 2012 as well as post-shot simulations. Fig. 8a shows the mean radius of the
measured primary neutron image, while Fig. 8b shows the measured relative deviation
from the mean radius along the polar direction.

278 the range of sizes and shapes collected to date. Given the current understanding of the
279 diagnostic, results are reported on the first two non-zero modes of the Legendre polynomial
280 fit to the contour at 17% of peak intensity.

281   Fig. 8a shows the summary of the hot-spot P_0^{hs} data, along with the corresponding
282 mean radii from post-shot simulated neutron images. Data values are indicated by the blue
283 (online) circles, while simulation values are indicated by red (online) squares. The values
284 of P_0^{hs} vary from 23.8 μ to 33.5 μm, with a mean of 27.4 μm, and a standard deviation
285 of 2.4 μm. The error on an individual measurement is $\sim$3-4 μm, with contributing factors
286 including: statistics, system resolution, aperture manufacturing, aperture pointing, and
287 inversion algorithm systematics[10,21]. Fig. 8b shows the summary of the hot-spot shape
288 measurements, expressed as the ratio, P_2^{hs}/P_0^{hs}. The values of P_2^{hs}/P_0^{hs} range between -0.37
289 and 0.21, with a mean value of -0.15 with a standard deviation of 0.21. Thus, the hot spot
290 volume of a typical implosion in 2012 may be characterized by an oblate spheroid with a
291 mean radius of 27.4 μm, and a radial deviation along the pole of -15%, or 4.4 μm.

292   Time integrated X-ray images, filtered to energies above $\sim$ 9 keV, were also collected
293 on this data set. Hard X-rays images indicate where the fuel assembly is hot, and should
294 be produce data consistent with the neutron image size and shape. As illustrated in Fig.
295 2b, equatorial X-ray images are collected along on a different line of sight, rotated 123°

15

₂₉₆ around the hohlraum axis from the neutron image, and thus projected asymmetries induce

₂₉₇ slight scatter in direct, shot-to-shot comparisons of P_0^{hs} and P_2^{hs} values. On average, the

₂₉₈ X-ray image P_0^{X-ray} is observed to be 27.3 μm, with 2.6 μm rms scatter, and the average

₂₉₉ P_2^{X-ray}/P_0^{X-ray} is observed to be -0.09 with an rms of 0.08, showing very good agreement

₃₀₀ with neutron image data.

₃₀₁ As indicated by the red (online) squares in Fig. 8a, synthetic primary neutron images

₃₀₂ were generated for comparison with data. Synthetic neutron images from different meth-

₃₀₃ ods of simulating implosions have been generated, including capsule only simulations,[22] as

₃₀₄ well as 2-D integrated hohlraum and capsule simulations.[23] The simulated images included

₃₀₅ here were generated by post-processing 2-D integrated hohlraum calculations, where the

₃₀₆ radiation drive seen by the capsule was tuned to match shock speed data from shock-timing

₃₀₇ experiments[24], radius vs. time data from convergent ablator experiments[25,26], and bang-time

₃₀₈ data from cryogenically layered dueterium-tritium implosions[5,6,11].

₃₀₉ Neutrons produced during the implosion are post-processed using a tool developed by

₃₁₀ Wilson[27] et al. that performs a 3-D Monte Carlo transport through the volume generated

₃₁₁ by revolving the 2-D mesh around the axis of symmetry. As the neutron exits the mesh, its

₃₁₂ position and direction are used to calculate the impact parameter in the plane orthogonal to

₃₁₃ the velocity. The resulting impact parameter image represents the Abel transformed source

₃₁₄ distribution. This 2-D distribution is further smoothed by a 10 μm Gaussian blur function to

₃₁₅ simulate a detector response. The tallies my be binned in energy to provide synthetic images

₃₁₆ of both the primary and scattered neutrons. Studies of these simulated scattered images

₃₁₇ have shown that the both the 10-12 MeV and 6-12 MeV energy images produce comparable

₃₁₈ contours of constant signal intensity and these agree well with the corresponding contours

₃₁₉ in density space. Further, the 17% of peak intensity contour represents a good estimate of

₃₂₀ the dense shell lateral extent. As can be seen in Fig. 8a, the simulation results show good

₃₂₁ agreement with the data, having a mean radius of $P_0^{hs} = 26.4$ μm, and standard deviation

₃₂₂ of 1.8 μm. On average the simulated images are symmetric with a $P_2^{hs}/P_0^{hs} = 0.01$, and a

₃₂₃ standard deviation of 0.18.
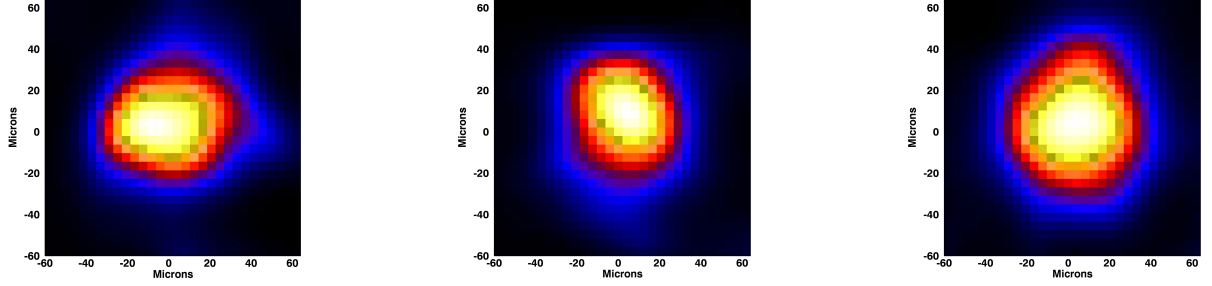
(a) Shot N111215: $P_0^{cf} = 43 \pm 6 \ \mu$m, (b) Shot N120321: $P_0^{cf} = 35 \pm 5 \ \mu$m, (c) Shot N120405: $P_0^{cf} = 43 \pm 3 \ \mu$m,

$P_2^{cf}/P_0^{cf} = -1 \pm 6$ % (10-12 MeV) $P_2^{cf}/P_0^{cf} = 1 \pm 6$ % $P_2^{cf}/P_0^{cf} = 12 \pm 6$ %

FIG. 9: Gallery of scattered neutron images from layered cryogenic implosions between Dec. 2011 and Aug. 2012.

B.   The Cold-fuel Image

Images of neutrons scattered to energies lower than 14.1 MeV are collected in a second camera system viewing the scintillator with its electro-optic shutter timed to coincide with neutrons in the 6-12 MeV energy window, except for shot N111215, which used a 10-12 MeV gate. For the 6-12 MeV image, this corresponds to a gate width of 241 ns starting 590 ns after bang time, and for 10-12 MeV the gate narrows to 55 ns. Simultaneous images with both cameras of a deuterium-tritium filled exploding pusher type capsule indicate that scattered images must be scaled in size by 6% to correct for a previously undetected magnification difference between the two camera systems. Fig. 9 shows a gallery of scattered neutron images, representing the range of sizes and shapes collected during 2012. As expected the scattered images are larger than the primary images, due to the dense deuterium-tritium volume surrounding the hot-spot. Further, absolute registration of the primary and scattered images shows that 17% contours of the two image are concentric with each other to a precision of $\pm$ 2.5 μm.

Fig. 10 shows a summary of the P_0^{cf} and P_2^{cf} measurements of this data set along with results of post-shot simulations of these experiments. Data values are indicated by the blue circles, while simulation values are indicated by red squares. Fig. 10a illustrates the variation of P_0^{cf} across the data set, with a minimum P_0^{cf} of 35 μm and a maximum of 46.6 μm. The mean P_0^{cf} value is 41 μm, with an rms scatter of 3.9 μm in the data. The error on an

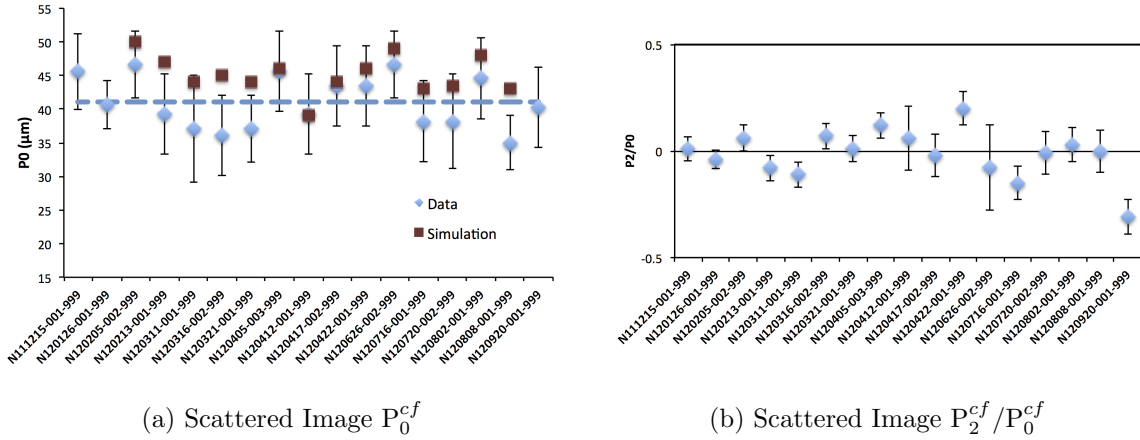(a) Scattered Image P_0^{cf} (b) Scattered Image P_2^{cf}/P_0^{cf}

FIG. 10: Scattered neutron image data from ignition experiments between Dec. 2011 and Aug. 2012 as well as potshot simulations. Fig. 10a shows the mean radius of the measured scattered neutron image, while Fig. 10b shows the measured relative deviation from the mean radius along the polar direction.

individual measurement is $\sim$5-6μm, depending on yield and with similar error contributions as the primary image. Fig. 10b shows the variation of the scattered image P_2^{cf}/P_0^{cf} in this data set. Similar to the primary image, the scattered image P_2^{cf}/P_0^{cf} varies from -0.31 to 0.2, but unlike the primary image, the mean value is -0.01 with an rms scatter of 0.11. Thus, in a typical 2012 layered implosion the volume of the deuterium-tritium payload near stagnation may reasonably be described as being contained within a sphere of radius 41 μm.

As mentioned, the red squares in Fig. 10a are the P_0^{cf} values from simulated images described above. The values range from a minimum of 39 μm to a maximum of 50 μm, with a mean value of 45 μm and an rms scatter of 2.8 μm. Although the simulated image sizes typically fall within an error bar of the data values, there is a clear systematic shift between the simulated scattered images sizes and the data. One possible explanation could be a systematic underestimate of the image size to due image statistics. Empirical characterization of the camera system, using image data from low yield implosions, *e.g* cryogenically layered tritium-hydrogen-deterium(2% at.)[4] capsules, as well as measured camera relative sensitivities, scintillator energy sensitivities, and estimates of scattering rates within the fuel assembly indicate the lateral extent of a cold fuel assembly with uniform density should be sufficiently sampled to produce a significant image at primary yields of $\gtrsim$ 1.0-1.5E14
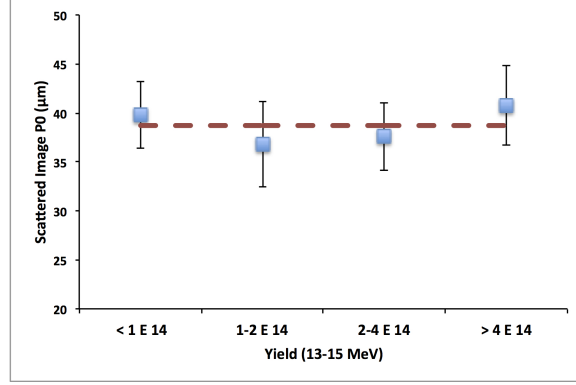
18

FIG. 11: Average scattered image P_0 within bins of neutron yield (13 -15 MeV). The red dashed line indicate the global average of 41 μm.

neutrons in the energy window from 13-15 MeV.

Fig. 11 shows the variation of the scattered image P_0^{cf} as a function of yield. The data in Fig. 10a has been averaged within the indicated energy bins, with at least three data points per bin. The error bars represent the rms scatter of the P_0^{cf} data within each bin. The red dashed line indicate the average value of 41 μm. These independent subsampled data points are consisted with the ensemble average and the hypothesis that the radius is not systematically underestimated due to statistics.

C. Dense Shell Geometry

In this simplified concentric shell model of the fuel assembly, the dense deuterium-tritium layer resides just outside the oblate spheroid defined by the hot-spot image and inside the sphere that is defined by the scattered fuel image. This volume may characterized by a mean thickness, T_0, and fractional deviation along the pole, $T_2/T_0 = (P_2^{cf} - P_2^{hs})/(P_0^{cf} - P_0^{hs})$. Fig. 12 shows the T_0 and T_2/T_0 data from 2012. Inferred shell thickness varies from a T_0 of 7 μm up to a maximum of 18.7 μm. The mean thickness across this data set is 13.6 μm, with an rms scatter across data of 3.9 μm. Because of the systematically oblate hot-spot, the shell thickness is systematically prolate with $T_2/T_0 = 0.27$ and $\sigma_{rms} = 0.34$. The consequence of the prolate shell is to effect a differential attenuation of the radial 14.1 MeV neutron flux between the pole the equator. The ratio of the polar to equatorial uncollided radial flux is given $(1-T_2/(2T_0))/(1+T_2/T_0) = 0.67$ for the typical fuel assembly above, which is consistent with nuclear activation diagnostic measurements.[28]

19

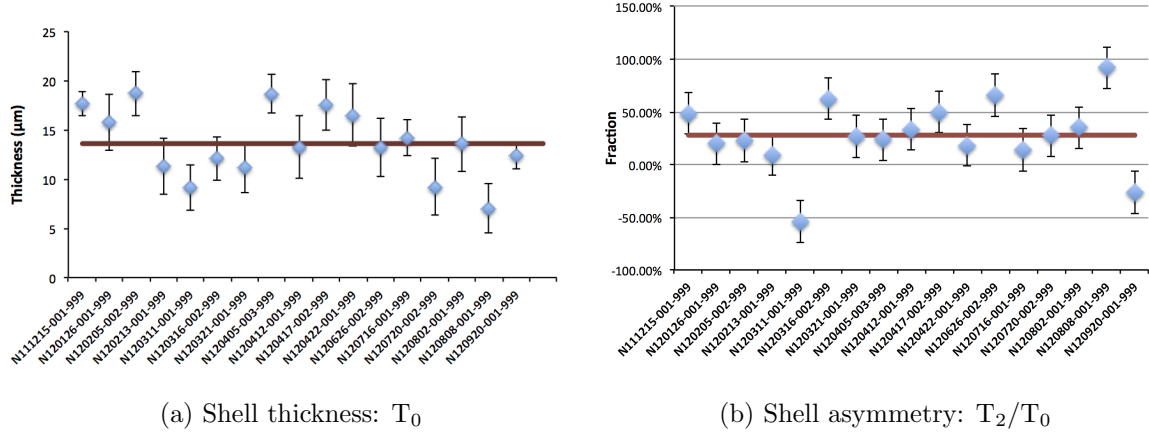(a) Shell thickness: T_0

(b) Shell asymmetry: T_2/T_0

FIG. 12: Dense deuterium-tritium shell geometry created by taking the difference between the Legendre polynomial expansion of the scattered image and hot spot image 17% of peak intensity contours.
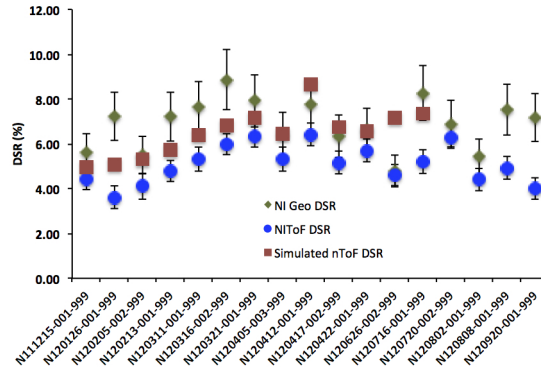

FIG. 13: Down scatter ratio data for layered cryogenic implosions. Blue circles are neutron time-of-flight measurements using a detector in front of the neutron imaging line-of-site, green diamonds are the inferred ratio using geometry data from the neutron imaging diagnostic, and the red squares are the results of 2-D integrated hohlraum simulations.

D. Geometric Downscattered Ratio

As described in section III B 2, the above geometry data may used to infer a geometric down scatter ratio based on the assumption that the deuterium-tritium fuel is uniformly distributed within the volumes calculated. The density of each region of the fuel assembly, hot-spot, and dense shell, is calculated using the initial deuterium-tritium mass, and the nuclear data for each shot, e.g., Yield, T_{ion}, and τ_{rh}, or gamma burn history. The inferred

geometric down scatter ratio data are shown in Fig. 13, indicated by the green diamonds. Also plotted in the figure are the time-of-flight down scatter ratio measurements, blue circles, using the NIToF detector which views the same neutron flux as the imager, as well as simulated down scattered ratios, red squares, using the post-shot simulations described previously. Although the geometric down scatter data trend with the time-of-flight data, they show a systematic excess over the time-of-flight data of 37%, with an rms variation of 25%. On average, the simulated neutron time-of-flight down scatter ratios show slightly better agreement with data, than the geometric results, but these too show a systematic excess of 27%.

Based on the simple model of the fuel assembly, there are three simple ways to ameliorate the discrepancy above: 1) increase the outer radius of the dense shell, 2) reduce the mass in the shell volume, or 3) a combination of both 1) and 2). For the inferred geometric data, the scattered image P_0^{cf} would need to increase 23.4%, or 9.6 μm, on average, to eliminate the discrepancy. This represents a $\sim 2\sigma$ systematic shift in the size of the image and as discussed above is inconsistent with the current understanding of system performance. Reducing the mass within the cold-fuel shell by 23.5% will also eliminate the discrepancy between the data and the geometric down scatter ratio, though this represents a significant fraction of the fuel assembly, close to 40 μg. Initial studies using 2-D Hydra simulations have indicated several possible means by which mass may be moved outside the 17% of peak density contour, which has been shown to give good agreement with the scatter neutron image contour. Low mode mass asymmetries, due to asymmetric drive conditions, generate density gradients that will leave the 17% contour in the same location as the uniform density configuration, but move as much as 20% of the dense deuterium-tritium mass outside this volume. In addition, simulations with high mode 2-D mix at the ablator-fuel interface impart a similar effect, moving as much as 50% of the mass outside the 17% of peak contour. In 3-D, correspondingly smaller growth factors are needed to produce the same effect. An observed by product of this interface mix in simulated neutrons images is hot-spot shape (P_2^{hs}/P_0^{hs}) variability on the scale of 10%, which is consistent with observed variations in the data. More simulation studies and experimental data are required to establish a firm understanding of the source of the scattering rate discrepancy, but leading causes have been identified and will continue to be explored.

V. SUMMARY

The neutron imaging system has shown itself to be a capable and productive diagnostic tool for understanding the performance of ignition experiments at the NIF. The system routinely produces high quality neutron images of where 14.1 MeV neutrons are born and scattered in imploded deuterium-tritium fuel assemblies. Primary neutron images have been collected at yields as low as 9E12, and both primary and scattered (6-12 MeV) neutron images have been collected on 17 cryogenically layered deuterium-tritium ignition experiments during the period from Dec. 2011 and Aug. 2012. Data from the neutron image diagnostic has been used to create a simple 3-D model of the compressed fuel assembly by rotating the 17% of peak intensity contour of both the images about the hohlraum axis. The resulting volumes show a typical ignition implosion produces a hot-spot that is characterized by an oblate spheroid with mean a radius of $P_0^{hs} = 27.4\mu$m, ($\sigma_{rms} = 2.4$ μm, and a polar deviation from the mean of P_2^{hs}/P_0^{hs} of -15%, ($\sigma_{rms} = 0.16$). X-ray images have a mean radius of $P_0^{hs} = 27.4\mu$m, ($\sigma_{rms} = 2.4$ μm, and a polar deviation of P_2^{hs}/P_0^{hs} of -0.11, ($\sigma_{rms} = 0.16$) showing excellent agreement with the neutron image data. Post-shot simulations, using integrated holhraum calculations, post-processed to generate synthetic neutron images, show good agreement with mean radius, $P_0^{hs} = 26.4\mu$m, ($\sigma_{rms} = 1.8$ μm), but tend to produce a symmetric implosions with P_2^{hs}/P_0^{hs} of -0.01, ($\sigma_{rms} = 0.18$). The corresponding scattered image generates an outer bounding surface for the fuel assembly that may be characterized by a sphere of radius $P_0^{cf} = 41$ μm, $\sigma_{rms} = 3.9$ μm, and P_2^{cf}/P_0^{cf} of -0.01, ($\sigma_{rms} = 0.11$). Simulated scattered image data are 10% larger, with $P_0^{cf} = 45$ μm, $\sigma_{rms} = 2.8$ μm, and P_2^{cf}/P_0^{cf} of -0.03, ($\sigma_{rms} = 0.10$).

The volume between these two surfaces, where the balance of the deuterium-tritium mass is located, is characterized by a shell with mean thickness $T_0 = 13.6$ μm, $\sigma_{rms} = 3.5$ μm, and a polar deviation of T_2/T_0 of 0.28, $\sigma_{rms} = 0.33$. Under the assumptions of a uniform density of deuterium and tritium in the shell volume, the hot-spot asymmetry will result in a radial polar flux to radial equatorial flux of 0.67, resulting in an asymmetric yield distribution. In addition, a simple concentric shell model may be used conjunction with other burn produced data and the assumption of fuel mass conservation to estimate the expected scattering rate from the assembly. This geometric based estimate of the neutron scattering rate within the fuel assembly is calculated to be 37% larger, on average than that observed by time-of-flight

22

detectors observing the same neutron flux. The shot-to-shot rms variation of this value is calculated to be 25%. The simulations used to produce the neutron image data predict a scattering rate that is 27% larger than observed in the data, with an rms value of 14%. Simulation studies have shown that the discrepancy between the geometric and simulated down scatter ratios may be explained by either low mode mass asymmetries with the fuel assembly, or possibly high mode mix at the ablator fuel interface. Further studies on these effect are underway.

ACKNOWLEDGMENTS

REFERENCES

[1] J. D. Lindl, *Inertial confinement fusion: the quest for ignition and energy gain using indirect drive* (Springer, AIP, New York, NY, 1998).

[2] S. W. Haan, J. D. Lindl, D. A. Callahan, D. S. Clark, J. D. Salmonson, B. A. Hammel, L. J. Atherton, R. C. Cook, M. J. Edwards, S. Glenzer, A. V. Hamza, S. P. Hatchett,

M. C. Herrmann, D. E. Hinkel, D. D. Ho, H. Huang, O. S. Jones, J. Kline, G. Kyrala, O. L. Landen, B. J. MacGowan, M. M. Marinak, D. D. Meyerhofer, J. L. Milovich, K. A. Moreno, E. I. Moses, D. H. Munro, A. Nikroo, R. E. Olson, K. Peterson, S. M. Pollaine, J. E. Ralph, H. F. Robey, B. K. Spears, P. T. Springer, L. J. Suter, C. A. Thomas, R. P. Town, R. Vesey, S. V. Weber, H. L. Wilkens, and D. C. Wilson, "Point design targets, specifications, and requirements for the 2010 ignition campaign on the national ignition facility," Physics of Plasmas **18**, 051001 (2011).

[3]O. L. Landen, J. Edwards, S. W. Haan, H. F. Robey, J. Milovich, B. K. Spears, S. V. Weber, D. S. Clark, J. D. Lindl, B. J. MacGowan, E. I. Moses, J. Atherton, P. A. Amendt, T. R. Boehly, D. K. Bradley, D. G. Braun, D. A. Callahan, P. M. Celliers, G. W. Collins, E. L. Dewald, L. Divol, J. A. Frenje, S. H. Glenzer, A. Hamza, B. A. Hammel, D. G. Hicks, N. Hoffman, N. Izumi, O. S. Jones, J. D. Kilkenny, R. K. Kirkwood, J. L. Kline, G. A. Kyrala, M. M. Marinak, N. Meezan, D. D. Meyerhofer, P. Michel, D. H. Munro, R. E. Olson, A. Nikroo, S. P. Regan, L. J. Suter, C. A. Thomas, and D. C. Wilson, "Capsule implosion optimization during the indirect-drive national ignition campaign," Physics of Plasmas **18**, 051002 (2011).

[4]M. J. Edwards, J. D. Lindl, B. K. Spears, S. V. Weber, L. J. Atherton, D. L. Bleuel, D. K. Bradley, D. A. Callahan, C. J. Cerjan, D. Clark, G. W. Collins, J. E. Fair, R. J. Fort-ner, S. H. Glenzer, S. W. Haan, B. A. Hammel, A. V. Hamza, S. P. Hatchett, N. Izumi, B. Jacoby, O. S. Jones, J. A. Koch, B. J. Kozioziemski, O. L. Landen, R. Lerche, B. J. Mac-Gowan, A. J. MacKinnon, E. R. Mapoles, M. M. Marinak, M. Moran, E. I. Moses, D. H. Munro, D. H. Schneider, S. M. Sepke, D. A. Shaughnessy, P. T. Springer, R. Tommasini, L. Bernstein, W. Stoeffl, R. Betti, T. R. Boehly, T. C. Sangster, V. Y. Glebov, P. W. McKenty, S. P. Regan, D. H. Edgell, J. P. Knauer, C. Stoeckl, D. R. Harding, S. Batha, G. Grim, H. W. Herrmann, G. Kyrala, M. Wilke, D. C. Wilson, J. Frenje, R. Petrasso, K. Moreno, H. Huang, K. C. Chen, E. Giraldez, J. D. Kilkenny, M. Mauldin, N. Hein, M. Hoppe, A. Nikroo, and R. J. Leeper, "The experimental plan for cryogenic layered target implosions on the national ignition facility—the inertial confinement approach to fusion," Physics of Plasmas **18**, 051003 (2011).

[5]S. H. Glenzer, D. A. Callahan, A. J. Mackinnon, J. L. Kline, G. Grim, E. T. Alger, R. L. Berger, L. A. Bernstein, and et al., "Cryogenic thermonuclear fuel implosions on the national ignition facility," Physics of Plasmas **19**, 056318–1 (15 pp.) (2012).

24

[6] A. J. Mackinnon, J. L. Kline, S. N. Dixit, S. H. Glenzer, M. J. Edwards, D. A. Callahan, N. B. Meezan, S. W. Haan, J. D. Kilkenny, and T. Doeppner, "Assembly of high-areal-density deuterium-tritium fuel from indirectly driven cryogenci implosions," Physical Review Letters **108**, 215005–1 (4 pp.) (2012).

[7] D. C. Wilson, C. R. Christensen, G. L. Morgan, M. D. Wilke, P. A. Bradley, and P. L. Gobby, "Goals for and design of a neutron pinhole imaging system for ignition capsules," Review of Scientific Instruments **74**, 1705–1708 (2003).

[8] G. Grim, C. Barnes, P. Bradley, C. Christensen, A. Hauer, G. Morgan, J. Oertel, M. Wilke, D. Wilson, C. Barrera, S. Haan, B. Hammel, J. Koch, R. Lerche, M. Moran, V. Glebov, T. Sangster, J.-L. Bourgade, L. Disdier, I. Lantuejoul, and O. Landoas, "Neutron imaging at the nif," Jour. de Phys. IV **133**, 913–918 (2006).

[9] M. D. Wilke, S. H. Batha, P. A. Bradley, R. D. Day, D. D. Clark, V. E. Fatherley, J. P. Finch, R. A. Gallegos, F. P. Garcia, G. P. Grim, S. A. Jaramillo, A. J. Montoya, M. J. Moran, G. L. Morgan, J. A. Oertel, T. A. Ortiz, J. R. Payton, P. Pazuchanics, D. W. Schmidt, A. C. Valdez, C. H. Wilde, and D. C. Wilson, "The national ignition facility neutron imaging system," Review of Scientific Instruments **79**, 10E529 (2008).

[10] F. E. Merrill, D. Bower, R. Buckles, D. D. Clark, C. R. Danly, O. B. Drury, J. M. Dzenitis, V. E. Fatherley, D. N. Fittinghoff, R. Gallegos, G. P. Grim, N. Guler, E. N. Loomis, S. Lutz, R. M. Malone, D. D. Martinson, D. Mares, D. J. Morley, G. L. Morgan, J. A. Oertel, I. L. Tregillis, P. L. Volegov, P. B. Weiss, C. H. Wilde, and D. C. Wilson, "The neutron imaging diagnostic at nif (invited)," Review of Scientific Instruments **83**, 10D317–10D317–6 (2012).

[11] C. Cerjan, "Tbd," Phys. Plasmas (Submitted).

[12] P. Bell, D. Bradley, and B. McGowan, "Nif neutron imaging system sdr," (2005).

[13] R. F. Wagner, D. G. Brown, and C. E. Metz, "On the multiplex advantage of coded source/aperture photon imaging," Proceedings of the SPIE **314**, 72–76 (1981).

[14] R. D. Day, P. M. Brooks, R. L. Edwardds, F. P. Garcia, G. P. Grim, A. N. Jr., D. W. Schmidt, R. C. Snow, and A. C. Valdez, "Fabrication of a 3 × 3 neutron pinhole array," Fusion Science & Technology **51**, 776–781 (2007).

[15] A. P. Dempster, N. M. Laird, and D. B. Rubin, "Maximum likelihood from incomplete data via the em algorithm," Journal of the Royal Statistical Society, Series B **38**, 1 – 38 (1977).

[16] L. A. Shepp and Y. Vardi, "Maximum likelihood reconstruction for emission tomography,"

Medical Imaging, IEEE Transactions on **1**, 113 –122 (1982).

[17]V. I. Gelfgat, E. Kosarev, and E. Podolyak, "Programs for signal recovery from noisy data using the maximum likelihood principle: I. general description," Computer Physics Communications **74**, 335 (1993).

[18]J. Briesmeister *et al.*, *MCNP–A general Monte Carlo code for neutron and photon transport* (Los Alamos National Laboratory, 1986).

[19]D. B. Pelowitz and et al., "Mcnpx users's manual, version 2.5.0," Tech. Rep. LA-CP-05-0369 (Los Alamos National Laboratory, 2005).

[20]D. C. Wilson, G. P. Grim, I. L. Tregillis, M. D. Wilke, M. V. Patel, S. M. Sepke, G. L. Morgan, R. Hatarik, E. N. Loomis, C. H. Wilde, J. A. Oertel, V. E. Fatherley, D. D. Clark, D. N. Fittinghoff, D. E. Bower, M. J. Schmitt, M. M. Marinak, D. H. Munro, F. E. Merrill, M. J. Moran, T.-S. F. Wang, C. R. Danly, R. A. Hilko, S. H. Batha, M. Frank, and R. Buckles, "Modeling the national ignition facility neutron imaging system," Review of Scientific Instruments **81**, 10D335 (4 pp.) (2010).

[21]N. Guler, P. Volegov, C. R. Danly, G. P. Grim, F. E. Merrill, and C. H. Wilde, "Simultaneous usage of pinhole and penumbral apertures for imaging small scale neutron sources from inertial confinement fusion experiments," Review of Scientific Instruments **83**, 10D316–10D316–3 (2012).

[22]D. Clark, "Tbd," Phys. Plasmas (Submitted).

[23]O. S. Jones, C. J. Cerjan, M. M. Marinak, J. L. Milovich, H. F. Robey, P. T. Springer, L. R. Benedetti, D. L. Bleuel, E. J. Bond, D. K. Bradley, D. A. Callahan, J. A. Caggiano, P. M. Celliers, D. S. Clark, S. M. Dixit, T. Doppner, R. J. Dylla-Spears, E. G. Dzentitis, D. R. Farley, S. M. Glenn, S. H. Glenzer, S. W. Haan, B. J. Haid, C. A. Haynam, D. G. Hicks, B. J. Kozioziemski, K. N. LaFortune, O. L. Landen, E. R. Mapoles, A. J. MacKinnon, J. M. McNaney, N. B. Meezan, P. A. Michel, J. D. Moody, M. J. Moran, D. H. Munro, M. V. Patel, T. G. Parham, J. D. Sater, S. M. Sepke, B. K. Spears, R. P. J. Town, S. V. Weber, K. Widmann, C. C. Widmayer, E. A. Williams, L. J. Atherton, M. J. Edwards, J. D. Lindl, B. J. MacGowan, L. J. Suter, R. E. Olson, H. W. Herrmann, J. L. Kline, G. A. Kyrala, D. C. Wilson, J. Frenje, T. R. Boehly, V. Glebov, J. P. Knauer, A. Nikroo, H. Wilkens, and J. D. Kilkenny, "A high-resolution integrated model of the national ignition campaign cryogenic layered experiments," Physics of Plasmas **19**, 056315 (2012).

[24]H. F. Robey, T. R. Boehly, P. M. Celliers, J. H. Eggert, D. Hicks, R. F. Smith, R. Collins,

26

M. W. Bowers, K. G. Krauter, P. S. Datte, D. H. Munro, J. L. Milovich, O. S. Jones, P. A. Michel, C. A. Thomas, R. E. Olson, S. Pollaine, R. P. J. Town, S. Haan, D. Callahan, D. Clark, J. Edwards, J. L. Kline, S. Dixit, M. B. Schneider, E. L. Dewald, K. Widmann, J. D. Moody, T. Döppner, H. B. Radousky, A. Throop, D. Kalantar, P. DiNicola, A. Nikroo, J. J. Kroll, A. V. Hamza, J. B. Horner, S. D. Bhandarkar, E. Dzenitis, E. Alger, E. Giraldez, C. Castro, K. Moreno, C. Haynam, K. N. LaFortune, C. Widmayer, M. Shaw, K. Jancaitis, T. Parham, D. M. Holunga, C. F. Walters, B. Haid, E. R. Mapoles, J. Sater, C. R. Gibson, T. Malsbury, J. Fair, D. Trummer, K. R. Coffee, B. Burr, L. V. Berzins, C. Choate, S. J. Brereton, S. Azevedo, H. Chandrasekaran, D. C. Eder, N. D. Masters, A. C. Fisher, P. A. Sterne, B. K. Young, O. L. Landen, B. M. V. Wonterghem, B. J. MacGowan, J. Atherton, J. D. Lindl, D. D. Meyerhofer, and E. Moses, "Shock timing experiments on the national ignition facility: Initial results and comparison with simulation," Physics of Plasmas **19**, 042706 (2012).

[25]D. G. Hicks, B. K. Spears, D. G. Braun, R. E. Olson, C. M. Sorce, P. M. Celliers, G. W. Collins, and O. L. Landen, "Convergent ablator performance measurements," Physics of Plasmas **17**, 102703 (2010).

[26]D. A. Callahan, N. B. Meezan, S. H. Glenzer, A. J. MacKinnon, L. R. Benedetti, D. K. Bradley, J. R. Celeste, P. M. Celliers, S. N. Dixit, T. Döppner, E. G. Dzentitis, S. Glenn, S. W. Haan, C. A. Haynam, D. G. Hicks, D. E. Hinkel, O. S. Jones, O. L. Landen, R. A. London, A. G. MacPhee, P. A. Michel, J. D. Moody, J. E. Ralph, H. F. Robey, M. D. Rosen, M. B. Schneider, D. J. Strozzi, L. J. Suter, R. P. J. Town, K. Widmann, E. A. Williams, M. J. Edwards, B. J. MacGowan, J. D. Lindl, L. J. Atherton, G. A. Kyrala, J. L. Kline, R. E. Olson, D. Edgell, S. P. Regan, A. Nikroo, H. Wilkins, J. D. Kilkenny, and A. S. Moore, "The velocity campaign for ignition on nif," Physics of Plasmas **19**, 056305 (2012).

[27]D. C. Wilson, T. N. Arhculeta, R. J. Aragonez, D. P. Atkinson, M. A. Barrios, S. H. Batha, D. E. Bower, D. K. Bradley, R. A. Buckles, D. D. Clark, D. S. Clark, D. J. Clark, J. R. Cradick, C. R. Danly, J. M. Dzenitis, O. B. Drury, R. D. Day, V. E. Fatherley, B. Felker, J. P. Finch, D. N. Fittinghoff, M. Frank, F. P. Garcia, G. P. Grim, R. A. Gallegos, S. M. Glenn, N. Guler, A. H. Hsu, N. Izumi, S. A. Jaramillo, O. S. Jones, M. I. Kauffman, G. A. Kyrala, S. L. Pape, S. N. Liddick, E. N. Loomis, S. S. Lutz, T. Ma, A. J. Mackinnon, R. M. Malone, M. M. Marinak, P. McKenty, D. Mares, D. D. Martinson, N. S. Meezan, F. E.

Merrill, M. J. Moran, G. L. Morgan, C. Munson, T. J. Murphy, J. A. Oertel, M. V. Patel, P. J. Polk, G. P. Roberson, D. W. Schmidt, S. M. Sepke, B. K. Spears, R. Tommasini, A. Traille, I. L. Tregillis, A. C. Valdez, P. L. Volegov, T.-S. F. Wang, P. Weiss, C. H. Wilde, and M. D. Wilke, "Comparison of neutron and x-ray emission from nif implosions," European Journal of Physics (Submitted to the current conference proceedings).

[28]J. Knauer, "Tbd," Phys. Plasmas (Submitted).